

Research Paper

Continuous Eulerian tool path strategies for wire-arc additive manufacturing of rib-web structures with machine-learning-based adaptive void filling

Lam Nguyen^{a,*}, Johannes Buhl^a, Markus Bambach^{a,b}^a Mechanical Design and Manufacturing, Brandenburg University of Technology Cottbus - Senftenberg, Konrad - Wachsmann - Allee 17, Cottbus D-03046, Germany^b Advanced Manufacturing Lab, ETH Zurich, Leonhardstrasse 27, 8092 Zurich, Switzerland

ARTICLE INFO

Keywords:

Additive manufacturing
WAAM
Lightweight structures
Adaptive void filling
Machine learning

ABSTRACT

Rib-web structures are used for lightweight design in various applications. The most prominent cases are found in aerospace engineering, where intricate structures are produced by forging and subsequent machining or by machining from solid blocks of material. Due to the large scrap rate involved in conventional manufacturing, rib-web structures are suitable applications for additive manufacturing (AM) processes. Among the AM processes, wire-arc additive manufacturing (WAAM) is highly suitable for rib-web structures due to its high deposition rate and the potential to manufacture large-size parts. In WAAM, the welding strategy greatly influences the properties and quality of deposited parts. With an increasing number of starts and stops, the danger of uneven material build-up and welding defects increases. Unfortunately, most rib-web structures do not represent Eulerian paths, i.e. they cannot be manufactured with a continuous welding motion, in which every edge is visited only once. This study presents a novel strategy for generating optimal tool paths for WAAM of lightweight rib-web structures, mitigating the disadvantages of discontinuous welding paths such as welding defects and uneven build-up. It is shown that doubling the number of welding passes on each edge of the rib-web structure turns non-Eulerian paths into Eulerian paths, which can be welded continuously. When two or more weld beads are deposited on each edge, the vertices of the rib-web structure may suffer from underfilling. It is shown that this can be avoided by a correction strategy, which consists in manufacturing the part once, evaluating the size of voids in the junctions, and computing a correction to deposit the required amount of material into the center of the junction. While this strategy may be used if a single part is considered, it is shown that the tool path correction to be applied to arbitrary junction geometries can be represented by a neural network that is derived from an experimental database consisting of representative junction types. With this approach, paths for any rib-web geometry can be generated, which saves lead time in variant-rich production. The paths proposed in this work avoid non-welding moves and may hence outperform even single weld-bed strategies in terms of welding efficiency.

1. Introduction

Wire-arc additive manufacturing (WAAM) processes have the potential to manufacture medium and large-size parts with high deposition rates at low costs [1–3]. WAAM processes are hence applicable to components such as rib-web structures, which are predominantly used as lightweight aerospace structures but also found in equipment used in heat, chemical and process engineering, where the ribs are used, e.g., to promote heat transfer. High-performance components are typically produced by forging and subsequent milling. Forged ribs are created by forming work pieces between two dies, and this process usually results in high tooling costs [4]. Very often, rib-web structures are manufactured by removing material from solid blocks, which yields a very

high buy-to-fly ratio [5] and material waste. Using WAAM processes to manufacture rib-web structures, thin-walled or honeycomb structures offers a high potential for reducing material waste, machining operations, investments into tooling and machinery, and production lead-time. Thus, WAAM processes are candidates for replacing these conventional manufacturing processes.

A WAAM process adopts either gas tungsten arc welding (GTAW) or gas metal arc welding (GMAW) to melt and deposit metallic wire. In GTAW, the wire is fed laterally which does not allow for direction-independent welding. Thus, more complex path strategies need to be devised and the welding efficiency is significantly lower than in GMAW. GMAW, therefore, is often chosen to implement WAAM. The electric arc melts the consumable wire electrode and the base material. The

* Corresponding author.

E-mail addresses: lam.nguyen@b-tu.de (L. Nguyen), johannes.buhl@b-tu.de (J. Buhl), mbambach@ethz.ch (M. Bambach).

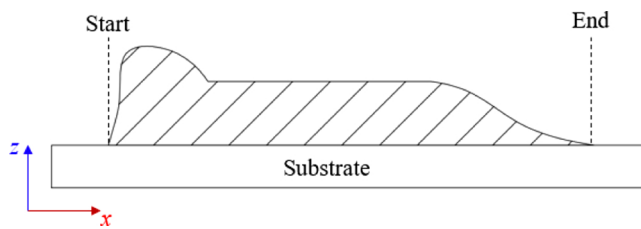


Fig. 1. Schematic cross section of a weld bead.

feedstock and substrate are heated intensively, which creates a non-uniform thermal expansion and contraction. These phenomena cause residual stresses. Consequently, deposited parts may show distortion, especially when the part size increases. The cold metal transfer (CMT) technology by Fronius is a variant of the GMAW process, which reduces the thermal inputs by 35–40 % [6,7]. Hence, residual stresses and distortion can be reduced [8], but not avoided. The weld bead geometry typically follows a profile as shown in Fig. 1, and shows a significant height difference between the start and end position. The penetration is lower at the starting point due to heat losses, thus the weld bead is higher than during steady-state welding. Towards the end position, a slope is observed due to the weld pool [9]. The accumulation of uneven geometries might lead to geometrical defects, under-fills, and a low surface quality.

To cope with the problem of uneven weld beads, many strategies have been proposed. A hybrid process has been developed that manufactures metallic parts using both additive and subtractive processes [10,11]. A milling operation was used to mill the surface between two subsequent layers. After depositing a layer, it was flattened and the accumulation of errors could be avoided. Zhang et al. [9] suggested a method to improve the deposition accuracy by controlling the welding parameters in the start and end portions of a weld track. For instance, the welding process started with a higher speed and decelerated to a constant velocity. Before reaching the end of the track, the velocity was decreased slightly. Ma et al. [11] proposed a method to deal with uneven weld beads. In their work, the welding direction alternated between adjacent layers. In addition to that, a reduction of the number of welding passes can be a remedy. Both raster and zigzag patterns could lead to warpage and anisotropy problems, and both turn out to be impractical for thin-walled components [12]. Contour path patterns have more benefits than zigzag patterns. Following contours of the part geometry, warpage and anisotropy can be reduced by changing the deposition direction regularly [13], and this tool path strategy is suitable for thin-walled structures [14].

Rib-web components consist of a number of connected ribs, and the deposition strategy has a great implication on the quality of the junctions between the ribs. A direct crossing strategy [15] can cause imperfections such as the development of material peaks and deposition failures in junctions. In other words, the welding torch works on existing seams, and thus the number of layers deposited at a vertex of the rib-web structure is larger than necessary. A common remedy is to deposit one wall continuously, while the walls intersecting this wall are deposited discontinuously, i.e., the torch moves over the vertex depositing material but leaves out the vertex itself. Stopping and starting the welding motion at a vertex may cause binding errors. To deal with this issue, the torch may follow a fillet at the intersection point instead of overlapping its neighbor ribs [16]. However, this strategy has a drawback since the generation of voids is possible; with fillet patterns, the intersecting area becomes larger and the deposited material is insufficient in this area. Venturini et al. [17] proposed a strategy to deposit rib-web structures with single weld beads, each rib was deposited by only one weld bead per layer. The tool path patterns are modified in junctions to deal with uneven weld beads.

Additional problems are encountered when rib-web structures are manufactured. Each layer of a rib-web structure can be represented by a graph. The multi-graph in Fig. 2 represents a schematic tool path for a rib-web component. It is not possible to weld the structure represented

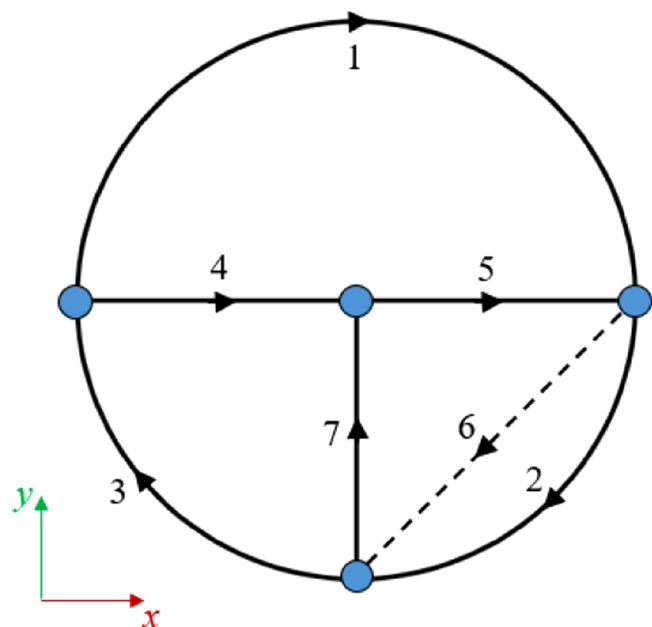


Fig. 2. Representation of a schematic tool path as a graph.

by the depicted graph in a single continuous motion of the weld torch. In other words, if the torch is allowed to travel along each edge of the graph only once, the welding torch cannot start and end at the same vertex. Jumping to a different position and re-igniting the arc there increases the danger of welding defects and under-fills. According to graph theory, the deposition process can be performed continuously if the tool path pattern represents an Eulerian path, i.e. a graph in which a continuous trail exists that visits each edge only once. A connected graph is Eulerian if and only if all vertices have an even degree, and semi-Eulerian if and only if two vertices in the graph have odd degree [18]. In graph theory, the degree of a vertex is the number of edges that meet at that vertex. Hence, in tool paths for rib-web structures, the degree describes the number of walls meeting at a vertex. Therefore, for arbitrary rib-web structures, no Eulerian path exists. In this case, the welding torch starts and stops more than once per layer, which increases the probability for welding defects.

A single weld bead width limits to about 11.0 mm [14]. To deposit thicker walls, two or multiple overlapping weld beads and oscillating patterns can be employed [11,19]. Multi-bead overlapping models are established by determining an optimal distance between two adjacent weld beads [14,20]. These models are constructed from the overlapping volume between single weld beads. A cross section profile of single beads is mathematically modelled as parabola, cosine or arc. Among the latter, the parabolic profile shows the best fit to real weld bead profiles [21]. Bead geometries can be represented using their height and width, which can be computed from the process parameters using algebraic equations [1,20]. Besides mathematical models, the weld bead geometry can also be predicted by using artificial neural networks (ANNs) [22,23] trained by experimental data using supervised learning. In this context, an ANN represents a relation between bead geometry and process parameters. The process parameters are adjusted to achieve the desired bead geometry. When straight walls are deposited, the cross section area derives from a single bead geometry. At turning points, the cross section of a single bead is irregular and unpredictable [19], thus the existing overlapping models are inapplicable in intersections and junctions occurring in rib-web structures.

Stair steps emerge between adjacent layers due to the parabolic shape of single weld beads. During finishing, the waviness has to be removed, e.g., by milling. Wavy surfaces thus yield a low deposition efficiency. Almeida and Williams [1] reported that the deposition efficiency for single bead walls is about 80 % with the GMAW-CMT process for Ti-6Al-4 V. With the same material, wire-plasma deposition reveals

a higher rate, averaging about 93 %. The surface waviness was captured on single thin-walled parts, and it was reported to be in the range of 0.35–1.51 mm [24].

The existing path planning strategies have not simultaneously resolved the problems of the uneven weld beads and voids in rib-web structures made by WAAM processes. Therefore, a tool path planning strategy with the following requirements is needed [25]:

- uneven weld bead geometry should be avoided
- productivity should be maximized by reducing rapid moves
- the algorithm should be simple and have low computation times
- customized wall thickness in the ribs shall be feasible
- valleys, and voids / underfillings shall be avoided at vertices

In this study, a new tool path strategy is put forward, aiming at improving the deposition quality for rib-web components. The welding torch follows continuous contour patterns defined as an Eulerian path for arbitrary connected rib-web structures, thus avoiding the drawback of starting and stopping in a layer. With this strategy, underfillings can occur at the vertices since each vertex is visited more than once. To avoid underfilling, an adaptive welding strategy has been developed to allow for dense vertices without voids. Section 2 details the materials and methods used in this work. It puts forward an analysis of the waviness and achievable wall thickness in single and double-bead strategies, showing that to achieve a certain wall thickness in ribs, two or more overlapping beads per layer are needed. Moving from a single bead to a double-weld bead strategy is shown to pave the way for creating Eulerian paths from any connected rib-web structure. This forms the basis of the tool path strategy detailed in section 3. The last section presents conclusions of the proposed method and the outlook.

2. Material and methods

2.1. WAAM system and feedstock

All WAAM experiments were conducted on the robot system shown in Fig. 3. A six-axis FANUC welding robot was used, which was synchronized with a two-axis positioner. As power source, a Fronius TPS500i welding system was utilized.

To operate the WAAM system, CAM (computer-aided manufacturing) programs are needed. The proposed tool path strategy contains two modules that are the tool path generation and the robot program generation. The tool path generation was developed in the software Rhinoceros®, which outputs continuous tool paths. The control points (vertices) from these paths are exported to an ASCII file. Table 1 depicts the output data of the proposed tool path strategy. The data include the ordinal number of the layer (No.), Cartesian coordinates (X , Y , Z), the orientation of the welding torch (Yaw, Pitch, Roll), and a Boolean variable, which controls the weld function. A script was developed in MATLAB® to generate robot programs from ASCII files.

Table 1
Output of the proposed algorithm.

No.	X	Y	Z	Yaw	Pitch	Roll	ON/OFF
1	0.0	10.0	0.0	0.0	0.0	0.0	True
1	10.0	10.0	0.0	0.0	0.0	0.0	True
.
.
n	0.0	10.0	0.0	0.0	0.0	0.0	False

Table 2
Chemical composition of ER70S-6 and C45.

Material	Element (Wt.%)					
	C	Mn	Si	P	S	Cr + Mo + Ni
C45	0.42	0.5	0.3	0.03	0.03	0.63 max
ER70S-6	0.06–0.15	1.4–1.85	0.8–1.15	0.025	0.035 max	0.63 max

Using the off-line programming software ROBOGUIDE®, the final robot program can be simulated and checked before starting the process.

Parts were built on carbon steel substrates C45 with 5.0 mm thickness. The chemical composition of the substrates and the electrode are reported in Table 2, according to AWS standard [26] and DIN EN 10083-1 [27], respectively. The process parameters are reported in Table 3. The stick-out is the length of the solid electrode extending from the tip of the nozzle, and it was kept constant (12.0 mm).

2.2. Evaluation of waviness and deposition efficiency

The WAAM process aims at manufacturing near-net shape geometries. For visible surfaces, it is necessary to apply post-processing, e.g. milling, to ensure accurate dimensions and good surface appearance. During process planning, CAD models need to be adapted for machining allowances [28]. The amount of material to be removed depends on the roughness and waviness of the surface. In this context, the waviness is used as a performance indicator to evaluate the quality of the surface. In WAAM, the surface properties are affected by the weld bead geometry. A wider weld bead leads to a rougher surface [29]. To evaluate the waviness, five walls of the mild steel ER70S-6 were deposited with a constant wire feed rate (5.2 m/min) and various levels of travel speed (100–20 cm/min). Material and WAAM system are described in section 2.1. Single weld beads of 100.0 mm length with 20 layers were deposited layer-by-layer. After each layer, the deposition direction was changed and the process paused for 5 s before resuming the deposition process.

The waviness (W_d) was computed according to DIN EN ISO 4287 standard as the greatest difference of amplitudes. The waviness was evaluated using macrographs. Specimens were extracted from the

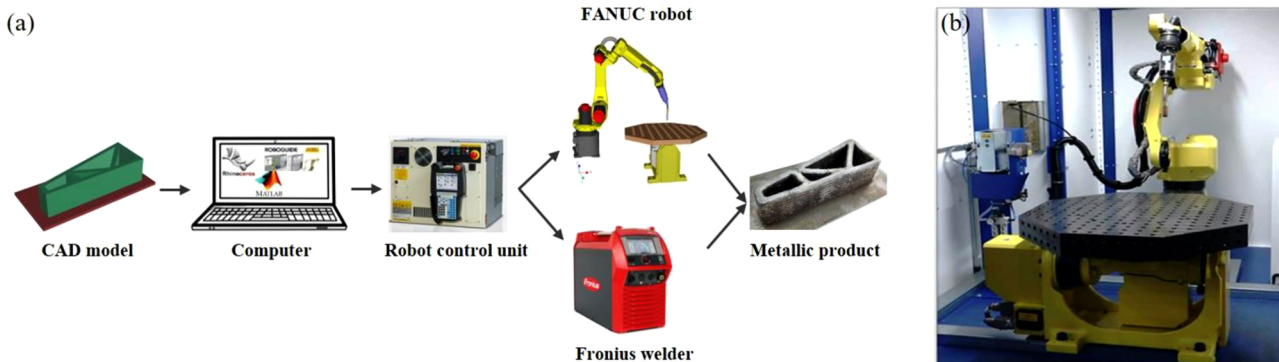


Fig. 3. (a) Illustration of the process chain and (b) WAAM robot system.

Table 3
Process parameters.

Process parameters	Value
Wire-feed rate (m/min)	5.2
Travel speed (cm/min)	40.0
Wire diameter (mm)	1.0
Shielding gas	80 % Ar and 20 % CO ₂
Gas flow (l/min)	15.0

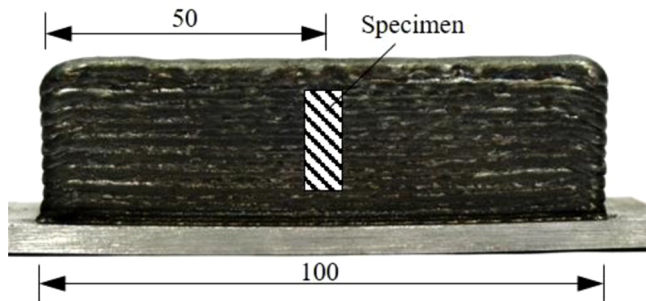


Fig. 4. Single wall at the travel speed of 40 cm/min.

center of the wall from the 4th layer upwards due to thermal instabilities in the first few layers [24], as shown in Fig. 4. A band saw was used to cut the walls with the thickness of 10.0 mm. The specimens then were ground and polished with grade P4000 sandpaper and 3.0 μm polishing paste, respectively. Macrographs were captured by means of the Leica DFC290 stereomicroscope and the DFC209 HD camera with magnification × 0.65.

Single weld beads have a certain thickness [14]. For thicker walls, a multi-bead strategy appears to be appropriate. Fig. 5 shows a schematic of a multi-bead overlapping model, the overlapping length between adjacent beads (l) is equal to two-thirds of the bead width (w) [20].

The following section presents a strategy to deposit walls with multiple beads. The proposed algorithm demonstrates the concept by using two weld beads to weld the ribs, allowing for creating Eulerian paths for arbitrary connected rib-web geometries.

2.3. Construction of Eulerian paths

Fig. 6 shows a graph representing a tool path for a rib-web structure. Four junctions are represented as four vertices. The welding torch follows a certain sequence of vertices to deposit the part. No Eulerian path

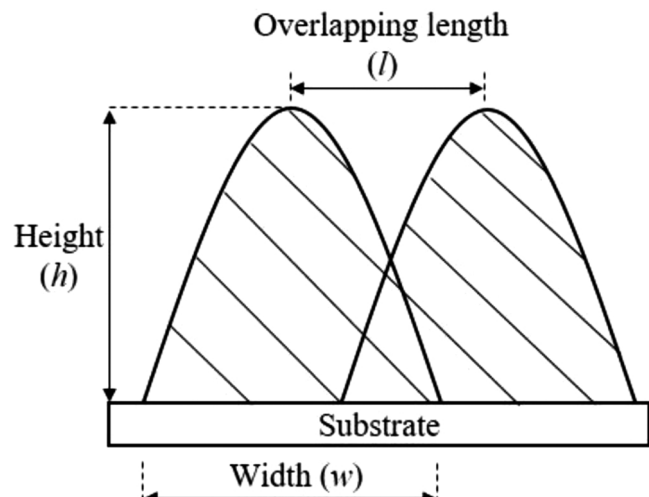


Fig. 5. A schematic of a multi-bead overlapping model, as reported by [20].

is feasible in this case. For example, the geometry may be deposited in two passes (Fig. 6a). Due to the rapid move, the processing time increases and imperfections may occur at the junctions. Additionally, the thickness of single-bead walls is limited to a certain range. Tool paths for arbitrary rib-web structures can be turned into Eulerian paths if the number of incoming and outgoing edges are equal at each vertex. This is achieved by moving twice along each edge, thus each vertex is visited twice as often as with a single-bead strategy and turned into a vertex of even degree, as shown in Fig. 6b. The tool path is continuous within a layer; the welding torch can start at any position and end at this position. Although the path is Eulerian, problems may occur when path lines cross at vertices. To avoid this issue, connector lines are introduced as shown in Fig. 6c. In this case, two path lines working on the same edge are cut and connected, thus four new vertices of degree two are generated. The proposed method yields continuous tool paths and aims at avoiding imperfections at vertices which may be encountered with the direct crossing strategy. The typical imperfections observed will be described later in the following section.

It is worth mentioning that the proposed strategy doubles the path length, which may result in a longer process time compared to a single bead strategy. However, typical wall thicknesses and machining allowances require a minimum wall thickness to be reached in as-deposited rib-web structures. For many applications, it thus seems justified to deposit two parallel weld beads in order to reach the desired thickness.

The strategy described above paves the way for computing continuous paths from the viewpoint of graph theory. To implement the strategy, the tool path lines need to be calculated from the part geometry. Parts are built from the bottom to the top, layer-by-layer. Thus, tool paths are also generated in this sequence. The slicing plane moves along the positive Z-direction with a step size corresponding to the layer thickness until there is no more intersection between the slicing plane and the CAD model, as shown in Fig. 7a. Fig. 7b shows a typical cross section between the slicing plane and the CAD model, consisting of three inner contour lines and a single outer contour line. An offset curve is generated for each contour curve, as shown in Fig. 7c. The distances of the contour lines to the original contour lines is chosen in such a way that the weld beads overlap in an appropriate manner to yield the desired wall thickness and a flat wall profile. The offset curves constitute the tool path for the current layer and the welding torch can follow these four contours to manufacture the wanted geometry, but the torch has to jump between contours. Hence, these contours need to be linked. To connect two closed curves, two connector lines are added, which are denoted as ‘connector lines’ introduced in Fig. 6. With n offset curves, the number of connector lines needed is $2(n - 1)$. To connect the contours, a random segment/edge of each offset curve is selected and the location of the connector lines is chosen randomly in-between one-third and two-thirds of the length of the selected segment. With a random allocation of the position of connector lines, traces on the part are avoided, which may occur if the connector lines were chosen at the same position on each layer. Traces generated this way are shown in Fig. 25a. As can be seen in Fig. 7d, a single closed curve is created which represents an Eulerian path.

However, it is important to note that adding two connector lines on the same edge is not allowed, as shown in Fig. 7e. In this case, two connected offset curves and a closed sub-path would be created on an edge. Such closed sub-paths must be avoided since they would make the tool path on the current layer discontinuous. To void this problem, a condition is added when selecting random edges for adding a connector line: each edge is selected one time only.

2.4. Void filling in junctions

2.4.1. A geometric solution for void filling

In the CMT welding process, the welding parameters are fixed, so that the weld bead geometry is supposed to be constant. As can be seen

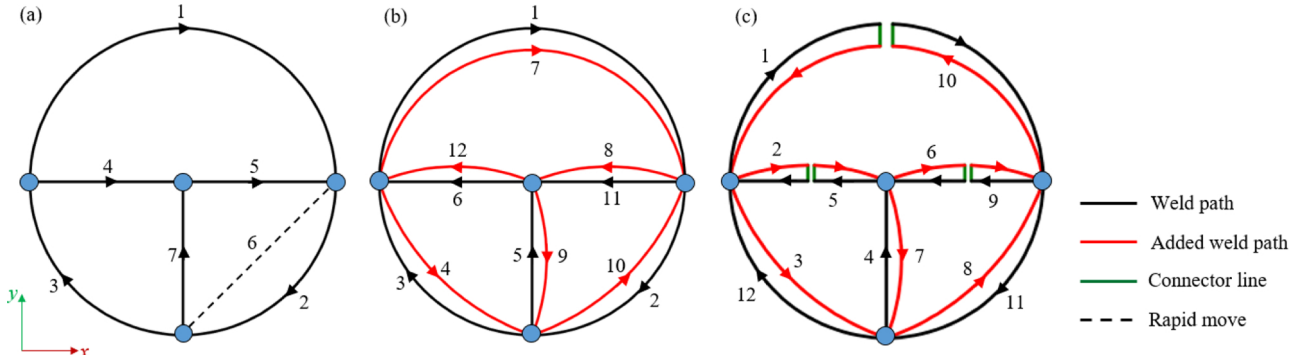


Fig. 6. Representation of the tool path by a graph: (a) single pass; (b) double pass without connector lines; (c) double pass with connector lines.

from Fig. 9, tool paths consisting of three contour paths may create underfillings (voids) inside the vertex of the rib-web structure. In this case, the material deposited is insufficient to fill the vertex. Depending on the angle between the two segments that meet at a vertex, the robot arm decelerates to follow the tool path precisely and performs a change in the direction of motion (command FINE). By changing velocity, the weld bead geometry is affected, which can cause overheating or excess material [30]. Therefore, it is important to keep the travel speed constant, and the FANUC robot used in this study allows to accomplish this through the continuous motion command (command CNT100) [31]. However, keeping the velocity constant results in a deviation from the targeted path. As shown in Fig. 8, the target point (V_i) cannot be reached by the tool center point (TCP) as this would require to stop the motion there before changing direction. Instead, the TCP moves to the nearby edge by interpolation. This inaccurate movement might lead to an underfilling if it is not compensated for each individual vertex geometry.

It is difficult to develop physics-based models for effectively resolving this problem. The lack of deposited material depends on the configuration of vertices, the material behavior, the part geometry (cooling is affected by radiation and convection), and the process parameters. To compensate the underfilling, a heuristic method is proposed. The tool path is actively corrected for sensitive vertices, i.e., the TCP is forced to move deeper into the center of the junction by changing the position of the vertices of the tool path. The remainder of this section deals with the question how to determine the position of the shifted vertex to achieve a precise deposition of material, avoiding underfilling as main defect.

Fig. 9 illustrates a typical tool path at a junction where three individual weld beads meet. APB is the tool path section for one of them. Let us assume that this section has been chosen in order to correct the deposited material volume. $A_oP_oB_o$ is an offset curve to APB with the distance l . The position of P is used to shift the turning point from P to P_N in the direction of P_o . The shifting distance depends on the vertex

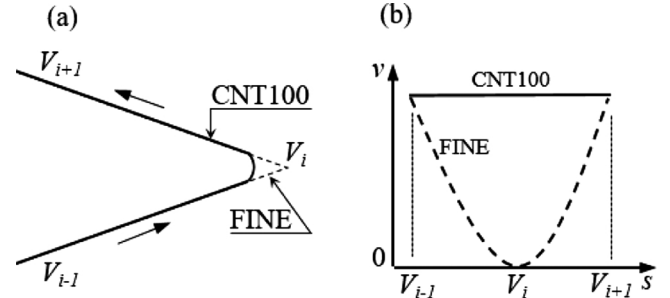


Fig. 8. Welding speed diagram at a turning point: (a) tool path pattern; (b) velocity diagram.

angle (θ). The smaller θ is, the farther P is shifted so that the deposited material fills the junction precisely.

Geometrically, the offset distance can be computed as:

$$\overline{PP_o} = \frac{l}{\sin(\theta/2)} \quad (1)$$

P_N is between P and P_o , and to ensure the overlapping length between two adjacent weld seams, P_oP_N is set to l .

$$\overline{PP_o} = \overline{P_oP_N} + \overline{PP_N} = l + \overline{PP_N} \quad (2)$$

From Eq. 1 and Eq. 2 the position of point P_N can be calculated as:

$$\overline{PP_N} = l \left(\frac{1}{\sin(\theta/2)} - 1 \right) \quad (3)$$

Let the points E and F denote the start and end points of the adapted path. These points are located on the original path and the distance between two points has been chosen to be equal to l . The location of the two points can be computed as:

$$\overline{PE} = \overline{PF} = \frac{l}{2 \sin(\theta/2)} \quad (4)$$

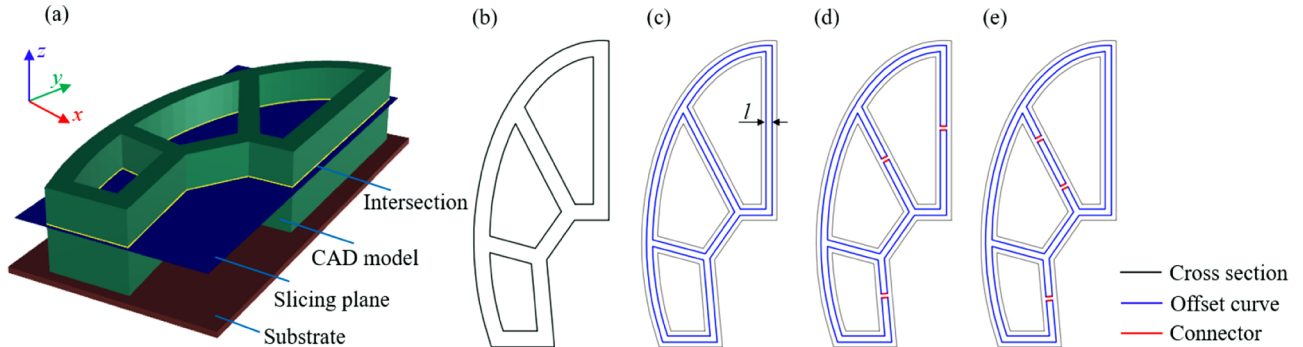


Fig. 7. Eulerian path generation: (a) illustration of the slice procedure; (b) cross section; (c) offset curves; (d) valid path; (e) invalid path.

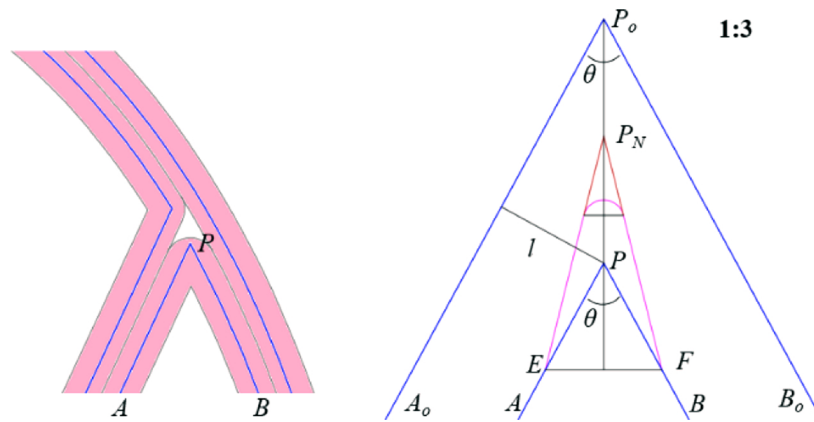


Fig. 9. A schematic of a basic adaptive void-filling path.

The TCP follows the path AEP_NFB instead of APB to fill the junction with material. The deposited volume depends on factors such as the configuration of the junction, the heat transfer properties, the deposited material, and the process parameters. Thus, the geometrical solution does not hold for arbitrary cases. To increase the reliability of the geometric approach, an empirical weight λ is introduced, which corrects the position of the point P_N :

$$\overline{PP_N^*} = \lambda \cdot l \left(\frac{1}{\sin(\theta/2)} - 1 \right) \quad (5)$$

To determine the value of λ , experimental tests are performed and the voids resulting from the welding experiments are evaluated. Let L indicate the measured length of the void resulting from a deficit of deposited material, then λ can be estimated from the measured value of L and the smallest angle of the conjunction (θ_{min}) as:

$$\lambda = \frac{l \left(\frac{1}{\sin(\theta_{min}/2)} - 1 \right)}{L} \quad (6)$$

Fig. 10 illustrates how L is determined. The considered junction has four arms with symmetrical geometry. The junction was deposited with 12 layers and the layer thickness was 1.8 mm. The material and process parameters are described in section 2.1. The part has a valley and two voids. A digital caliper was used to measure the length of the valley, which yields $L = 28.3$ mm. The empirical weight λ is computed once using the geometrical relation given by Eq. 6, and it is used to calculate the shifting distance ($\overline{PP_N^*}$) for the selected turning point.

The proposed method was validated further to evaluate the feasibility and the efficiency of the geometrical correction. Various junction geometries were welded with and without the correction. As shown in Fig. 11, four different configurations were investigated. Metal parts were manufactured and machined to observe and analyze the created

surfaces. Destructive testing is typically not feasible in production. Rather, non-destructive methods should be used to analyze the existence of voids, such as radiography [32] and ultrasonic inspection [33]. With non-destructive methods, the process of controlling the quality of junctions may be integrated in quality control during production.

Using the proposed method, each junction type first needs to be produced once to determine the correction needed. This approach seems feasible if series production of a single part is performed. For variant-rich production of various shapes, it does not seem justified to manufacture a part such that a corrected part can be produced. The main question to be answered is how to design a rule-based method to obtain L for an unknown junction geometry. The following section presents the chosen approach for predicting L and hence the correction factor λ from a data-driven neural network to perform defect-free welding of arbitrary rib-web geometries. In order to keep the effort for creating experimental training data as low as possible, the process parameters are fixed and the number of ribs at the junction is limited to at most four.

2.4.2. Machine learning approach for void filling

2.4.2.1. Tolerance for the shifting distance. Valleys and voids can be compensated through measuring L from experiments. When $\overline{PP_N^*}$ is larger than L , voids are compensated. The essential point is to find the smallest value of $\overline{PP_N^*}$ which ensures that no voids are created at the junction. To determine the lower limit, the junction in Fig. 10 was used, and $\overline{PP_N^*}$ increased gradually from 0.0–30.0 mm by 1.0 mm. After depositing 12 layers, the resulting specimens were milled flat from top to bottom with a depth of cut of 0.5 mm until voids were visible. The possible void area (A_{void}) was measured by means of a Leica DFC290 stereomicroscope and a DFC209 HD camera at a magnification $\times 0.65$. The lower limit is used as the tolerance for machine learning results.

2.4.2.2. Training an artificial neural network. L is used to calculate λ , which is used for computing the shifting distance at turning points. This section presents a supervised machine learning approach to predict L from the configuration of the junction. From the models used in machine learning, artificial neural networks (ANN) seem to be suitable for representing the shifting distance from data obtained experimentally. The ANN makes predictions from rule-based learning with training data. In this case, the training data are the number of turning points (η) and the configuration of junctions. With three and four ribs meeting at a junction, there are mainly eight groups of junctions, as shown in Fig. 12, and the maximum number of angles is four. Junctions are categorized via the number of equal angles.

Using the ANN, L can be expressed as a function of η , and the four angles:

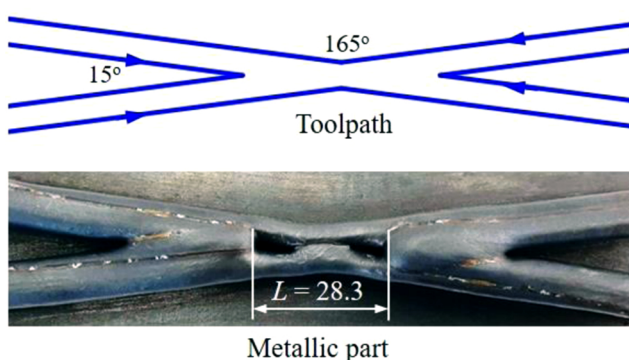


Fig. 10. A presentation of determining L with standard contour tool path.

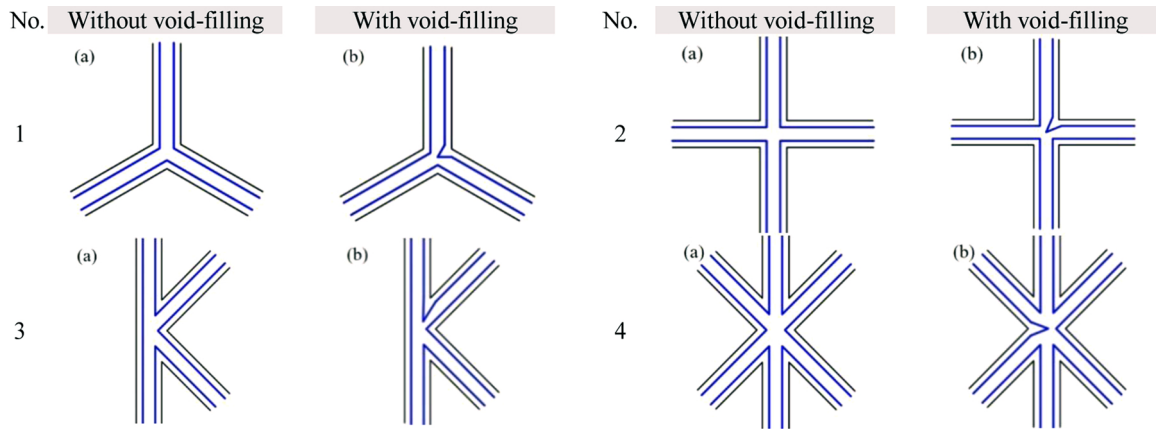


Fig. 11. A comparison between standard contour tool path (a) and corrective contour tool path (b).

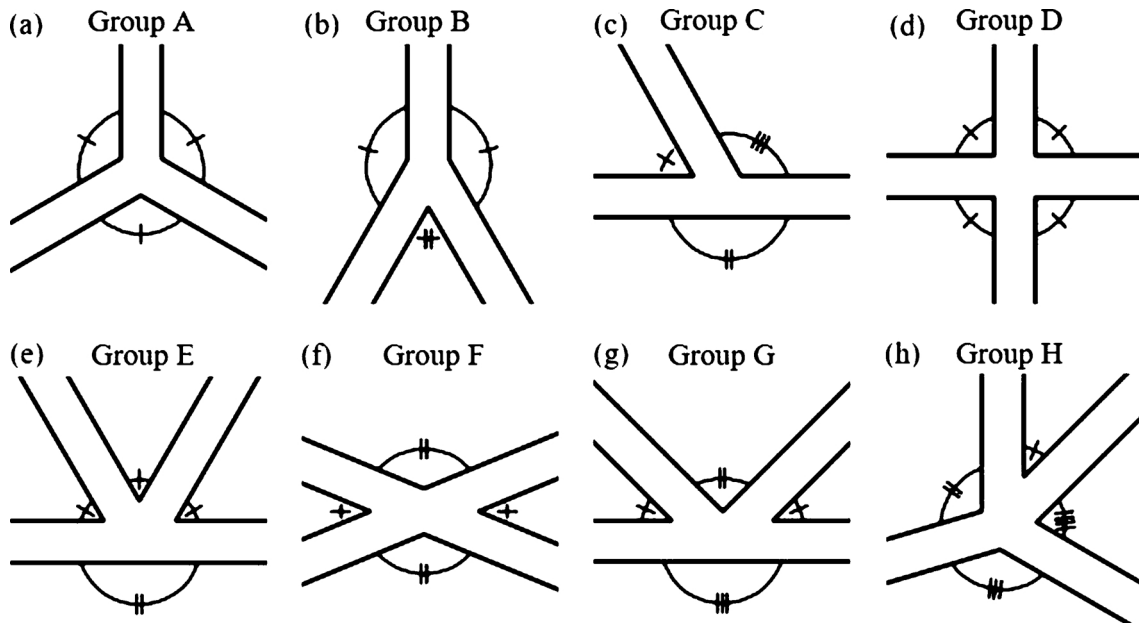


Fig. 12. Types of junctions considered; (a) three ribs with three equal angles; (b) three ribs with two equal angles; (c) three ribs with different angles; (d) four ribs with four equal angles; (e) four ribs with three equal angles; (f) four ribs with two-pair of equal angles; (g) four ribs with one-pair of equal angles; (h) four ribs with different angles.

$$L = \text{net}(\eta, \theta_1, \theta_2, \theta_3, \theta_4)$$

(7)

For instance, there is one only case with three turning points and three equal angles. To parameterize a junction, the angles are arranged so that θ_1 is the largest angle. All 63 junction geometries were defined and welded. The full data can be found in Appendix A. 60 random geometries were used to train the ANN and the remaining 3 geometries were used for validating the ANN. Each junction was deposited with five layers with the process parameters reported in section 2.1. A digital caliper was used to measure the length of the resulting voids. With the value of L obtained from welded specimens, all junctions with 12 layers were deposited with adaptive void-filling paths to validate the proposed method. It turned out that there was no occurrence of valleys and voids.

The training was performed using MATLAB® with the *nntrainool* tool. Fig. 13 depicts the ANN architecture. The ANN has three layers: input, hidden, and output layer. The ANN has five inputs and one output. From computational experiments, it was found that two hidden layers with 7 neurons showed a suitable network architecture. The training algorithm used was Bayesian Regularization [34], which showed the best performance among several tested algorithms.

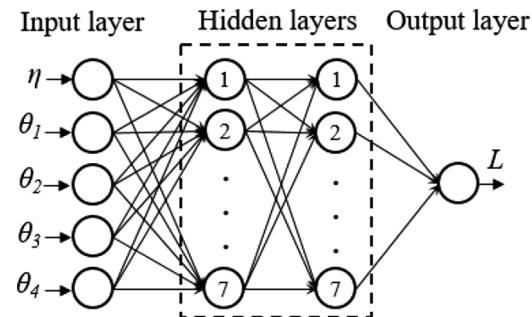


Fig. 13. Schematic architecture of the ANN.

2.5. Validation of the proposed method

Fig. 14 shows the CAD model of a validation case for the proposed tool path generation method. The part is 45.0 mm high. The dimensions of the rib-web structure are detailed in Fig. 14b. The tool path for printing the part was generated using the developed algorithm. Tool path generation proceeds layer by layer. The slicing plane slices the

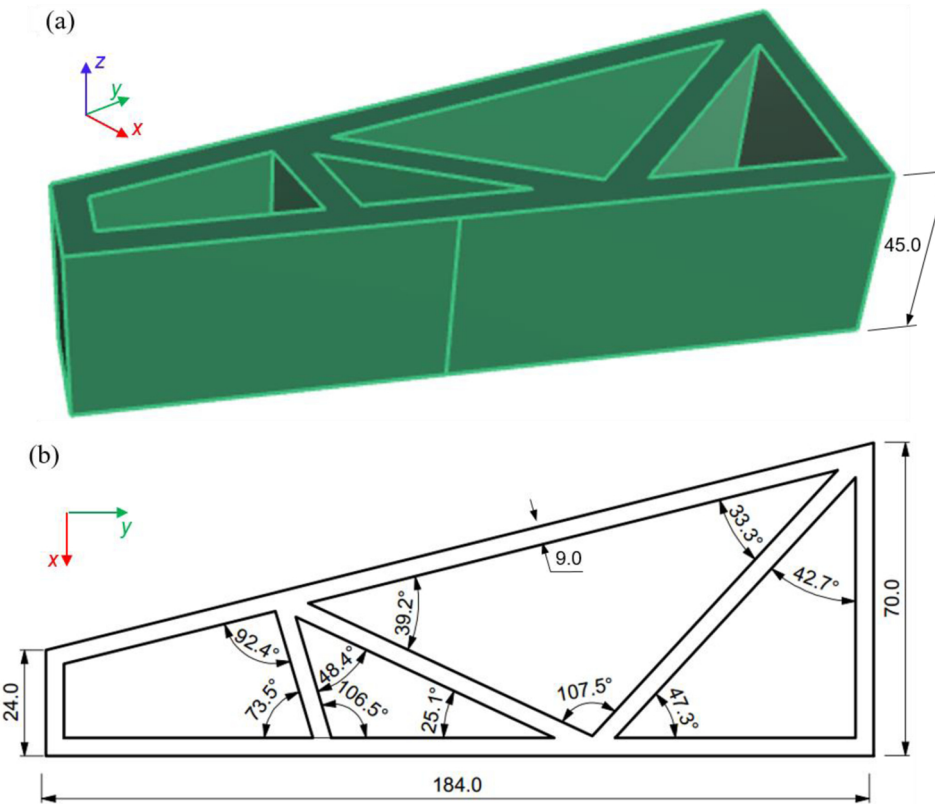


Fig. 14. CAD model of the case study: (a) perspective view of the CAD model; (b) a typical intersection.

CAD model from the bottom to the top with uniform distance in Z + direction. Based on the intersection between the slicing plane and the CAD model, inner and outer contours are obtained. The developed algorithm computes offset curves from inner and outer part contours, and then establishes the continuous tool path for each layer according to the proposed algorithm. The proposed method is applied for each intersection and connector lines are randomly allocated to avoid traces on the part.

3. Results and discussion

3.1. Evaluation of waviness and effective wall thickness

Fig. 15 illustrates macrographs of single-bead walls welded with different travel speeds (v_t). The bead width ranges from about 3.0 mm–7.0 mm and the waviness increases accordingly from around 0.3 mm to 0.6 mm. With double beads, the wall thickness ranges from about 5.4 to around 11.7 mm. For example, at the travel speed of 40 cm/min, the bead width is about 5.3 mm, the overlapping length is about 3.6 mm for multi-bead deposition, and thus the calculated wall thickness is approximately 9.0 mm with two overlapping beads. A two-bead wall (100.0 mm in length) was deposited using two parallel weld beads over 20 layers in height. Fig. 16 depicts a macrograph for the two-bead wall at the chosen travel speed. The measured wall thickness is about 9.0 mm and the waviness compares to those obtained with a single bead. It can be stated that multi-bead deposition does not affect the waviness.

The deposition efficiency (E) is computed as the ratio of the total remaining material and the deposited material, according to Jhavar et al. [35]. The deposition efficiency is above 82 % for single-bead walls, and this efficiency is higher for multi-bead deposition. For instance, about 94 % is the deposition efficiency for the two-bead walls at $v_t = 40$ cm/min.

3.2. Evaluation of the geometrical void filling criterion

Fig. 17 compares the performance of the standard contour tool path and the adaptive void-filling tool path with configuration of Fig. 10. As can be seen, the former depicts a valley and two voids. Based on the distance L , λ is calculated. The junction has four turning points and one is selected to perform the tool path correction at each layer. With the adaptive void-filling tool path, the metallic part reveals no voids.

Welding the geometry once using only the contour lines and determining the distance L is cumbersome in practice. Due to the complex dependence of L on the junction geometry, material, and process parameters, the correction factor λ cannot be calculated by a model without using experimental data. Appropriate data sets can be used to train a neural network, as shown in the subsequent section, which allows for calculating the correction for cases which are not included in the training set.

Fig. 18 shows the side view of the metallic parts from Fig. 17. There is a deviation (Δh) between the target height and the actual height at the junction. When a peak in the deposited junction occurs, Δh is positive and vice versa. Ideally, Δh is close to 0. The original strategy yields a valley, and Δh is negative due to lack of material at the junction. In contrast, the junction welded with the adapted path reveals a peak because of excessive deposited material. When the height of the rib-web structure is low, peaks may not add up to a height that would jeopardize the welding process, i.e. small peaks can be tolerated, voids not.

The validation cases defined in Fig. 11 are shown in Fig. 19 below. The junctions were deposited with 12 layers and the process parameters reported in Table 3. As can be seen, the standard contour tool path does not deposit sufficient material to fill up the junctions, so that voids appear. The configuration with three ribs has a small void while the configuration with six ribs shows a larger void. Among the junctions with four ribs, the k-shaped configuration has a larger void than the cross-shaped one. In all cases considered here, the voids can be

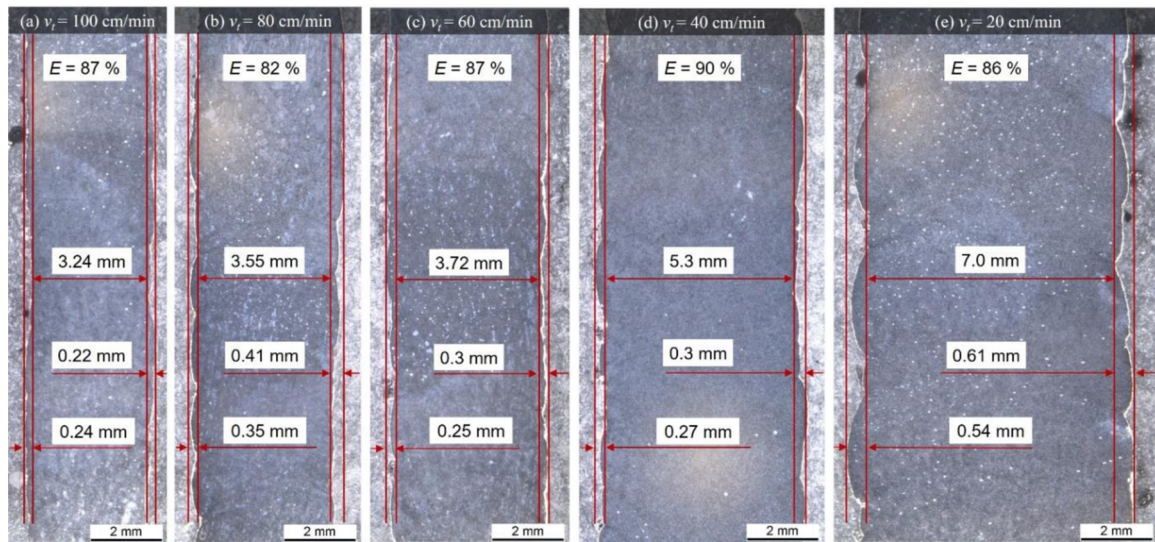


Fig. 15. Macrographs of the wall cross sections: (a) $v_t = 100 \text{ cm/min}$; (b) $v_t = 80 \text{ cm/min}$; (c) $v_t = 60 \text{ cm/min}$; (d) $v_t = 40 \text{ cm/min}$; (e) $v_t = 20 \text{ cm/min}$.

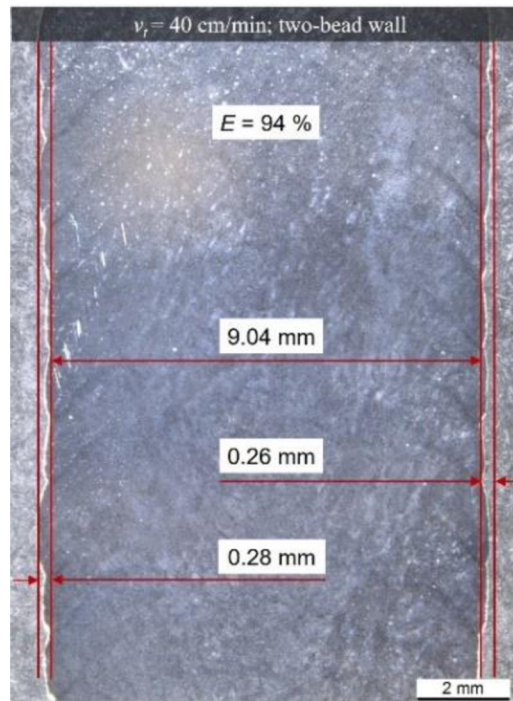


Fig. 16. Macrographs of the two-bead wall cross sections.

compensated by adapting the tool path, showing that the correction strategy is successful.

3.3. Performance of the ANN

3.3.1. Tolerance

Fig. 20 shows four typical cases with different PP_N^* . The void is smaller with increasing length of PP_N^* . There are two large voids with the original tool path, and a small void for $PP_N^* = 26.0 \text{ mm}$. The metallic part experiences no voids for $PP_N^* = 27.0 \text{ mm}$. The lower tolerance is the difference of the most suitable values for PP_N^* and L , which is -1.3 mm.

Fig. 21 shows the influence of the shifting distance on the void area. As can be seen, A_{void} experiences a drop from about 21.0 to 0.0 mm^2

when increasing PP_N^* from 0.0–27.0 mm. At the point where L attains the red line, there are no voids. This junction is one of the most essential junctions in rib-web structures; thus, the found lower tolerance in this case is considered as the general lower tolerance for all conjunctions and it shows the most with the reported process parameters.

3.3.2. Training ANN with experimental data

Fig. 22 shows the relationship between output and target through scatter plots. The scatter plot displays values of typically two variables for a set of data. In particular, the horizontal axis indicates the desired values, which are experimental data, and the vertical axis represents the predicted values obtaining from the ANN. Ideally, the experimental values and the predicted values are equal, and the perfect trend line is an inclined line at an angle of 45° (dashed lines in Fig. 22), which is quantified by an R-value of 1.0 in this case. However, R-values do not comprehensively indicate the prediction performance, even when they are significant. The adverse effect of large R-values is the problem of overfitting. This happens when the transfer function creates weights and biases, which can only predict existing data well, but not foreign data [36,37]. Overfitting of ANN can be problematic in machine learning. To verify whether the ANN is overfitted or not, three junctions were selected randomly from the full training data and those were not used in the training process, 60 training junctions were used to establish the ANN and the three remaining junctions were used for validation, as shown in Appendix B. As can be seen from Fig. 22, R-values reveal large values, which are close to 1.0. It can be stated that the ANN established proper rules between input and output layer.

Table 4 shows the validation results. The deviation between output and target is denoted as ΔL . The three junctions were selected randomly from the sample data, and they were not used for training the ANN. The ANN was able to predict new data, and the difference is within 1.0 mm. The ANN has significant R-values and it does not show overfitting. As a result, the ANN is able to predict the length of valleys with foreign configurations.

3.3.3. Determining of an optimal training data set

Fig. 21 shows the influence of the shifting distance on the void area. As can be seen, A_{void} experiences a drop from about 21.0 to 0.0 mm^2 when increasing PP_N^* from 0.0–27.0 mm. At the point where L attains the red line, there are no voids. This junction is one of the most difficult to weld junctions in rib-web structures due to the shallow intersection angle; thus, the found lower tolerance in this case is considered as the

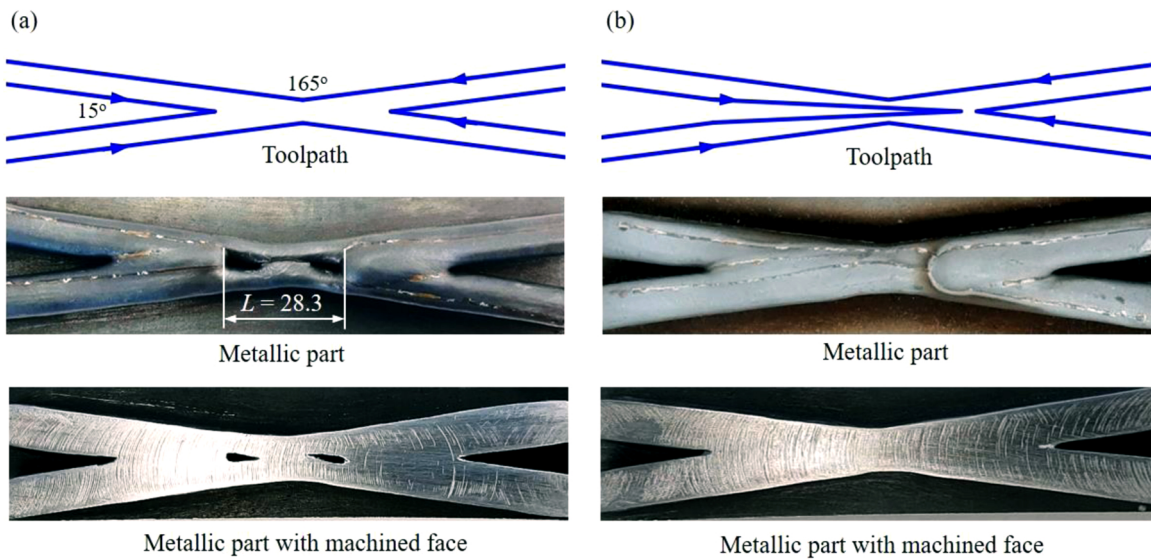


Fig. 17. Performance of an example: (a) tool path pattern without correction; (b) tool path pattern with correction.

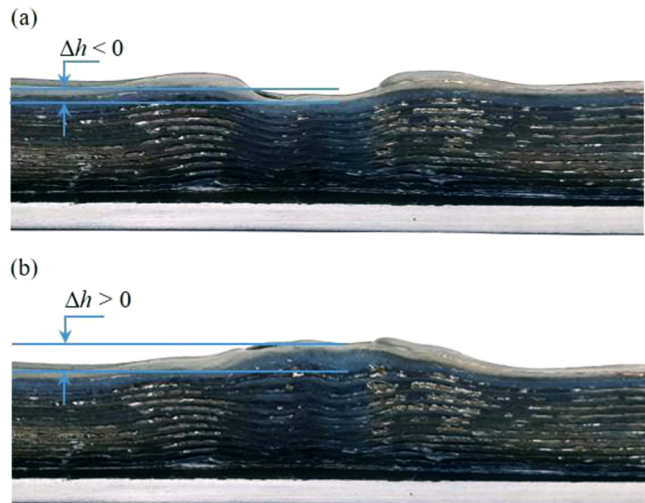


Fig. 18. Side view of the metallic part: (a) without correction; (b) with correction.

general lower tolerance for all conjunctions.

Generating samples is costly and time-consuming. Based on the full data set of 63 welded junctions, this section presents a procedure to

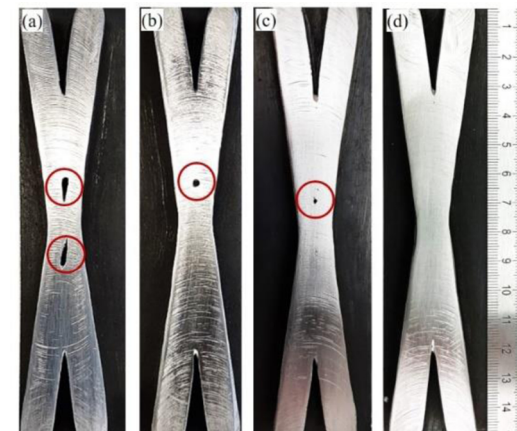


Fig. 20. Junctions with different PP_N^* : (a) 0.0 mm; (b) 25.0 mm; (c) 26.0 mm; (d) 27.0 mm.

select an optimal training data set. The idea is to design a training data set, which satisfies certain conditions. As stated above, the maximum allowable lower tolerance is -1.3 mm, and every prediction, which has a prediction error (ΔL) that is higher this value is accepted. To determine the sample size, draws from the full sample set were generated

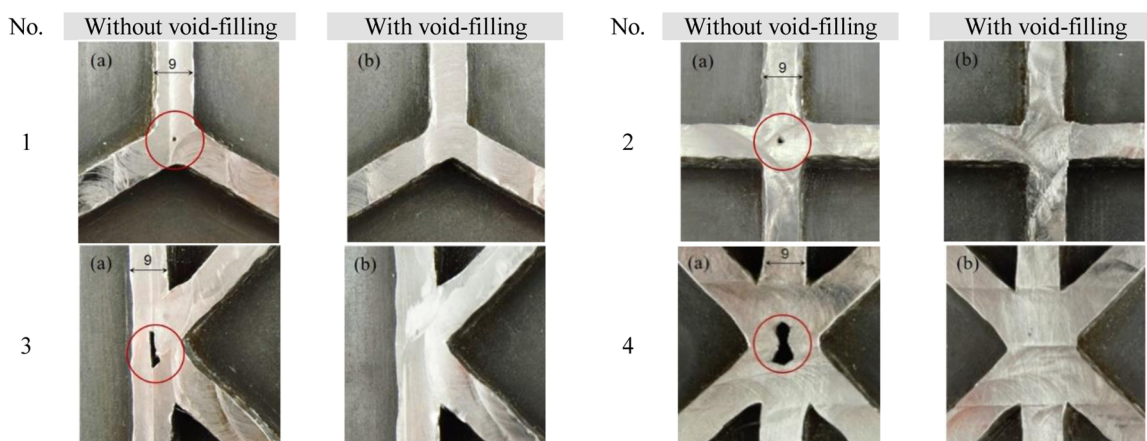


Fig. 19. Results for various junction geometries: (a) standard contour tool path; (b) adaptive void-filling tool path.

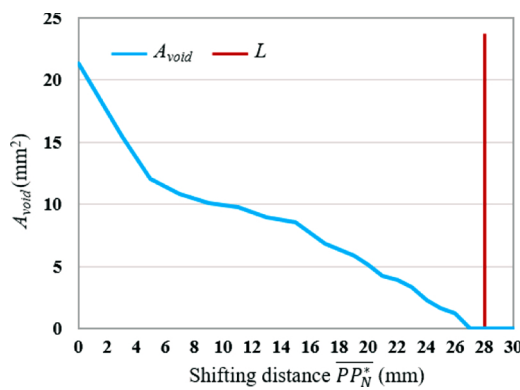


Fig. 21. Influence of shifting distance on void area.

randomly without repetition. The draws were used to train the ANN and the remaining data sets were used to validate the performance of the ANN. The process of picking and training took place with a maximum of 1000 repetitions. As soon as the results met the constraint, the process was stopped.

Initially, 60 junctions were used for training, and three were used for validation. The process continued by reducing the number of training sets by one unit until ΔL could not meet the condition. At 45 junctions, it was impossible to establish an ANN, which met the requirement, and thus 46 sampling data sets was considered as the optimal sampling set size, as shown in Appendix C. The first 46 samples are training data and other 17 are used for validation.

Fig. 23 presents the error histogram of six typical trials through the optimization process. Most errors distribute from -1.2 to 0.8 mm. The first trial has the best performance, the errors range from -1.2–2.8 mm. The distribution range of errors tends to be larger when reducing the number of training data. By reducing the number of training data sets from 63 to 46, the process of collecting data is simpler and less expensive.

While the proposed classification scheme for junction types can be applied to arbitrary rib-web structures (defined by graphs), it is worth noting that the minimum number of junction types that was identified here to train the ANN may not be sufficient if the method is transferred to other materials and experimental set-ups. However, for a new material or a different experimental set-up, one may start with the 46 cases defined as optimum training set and use additional validation cases to analyze whether a void-free deposition is achievable. If this is not the case, one may include the cases used for validation into the training data set and repeat the training. In this case, a new validation set is needed. Choosing new test data for validation and adding them to the

Table 4
Validation of the ANN.

No.	Group	Target (mm)	Output (mm)	ΔL (mm)
1	F ₇	24.5	24.42	-0.08
2	H ₃	5.5	6.3	0.8
3	H ₁₅	7.0	7.93	0.93

training data in case the required accuracy of the ANN has not been met may be repeated as long as it is required to achieve the desired model accuracy for void-free deposition.

It is clear that the effort for training the ANN should only be taken if a variety of part geometries is to be produced. If the WAAM system is used in variant-rich production of rib-web parts, it seems expedient to cover all possible cases by training an ANN, so that production of a new variant can be accomplished with minimal lead time. In contrast, if the WAAM system is always used to manufacture the same rib-web geometry, one may arrive at a void-free deposition process by manufacturing a single part based on the geometrical correction proposed above, which will yield underfillings. Measuring the length L of the void in each vertex then allows to calculate a correction that will enable successful manufacture of the part without voids.

3.4. Validation results

Fig. 24 depicts the tool paths for the case study used to validate the proposed approach. A standard contour tool path and the proposed Eulerian tool path are compared. The standard method produces a great number of passes. The welding torch switches on and off several times in each layer. This might lead to welding defects or imperfections due to uneven weld beads. The junctions might show voids and these voids reduce the performance of the part. The proposed method, in contrast, produces only one single welding pass per layer. Basic contour patterns are connected to create an Eulerian path, and the adaptive void-filling path is applied to each junction with the ANN obtained with the optimal training data set.

Table 5 compares the number of weld passes and the process time of both strategies. Due to transition lines between contours, the processing time with the standard tool path was about 21 % higher than the one with the proposed Eulerian tool path. The welding torch switched on and off frequently, and sometimes there were machine errors because of slag emerging on the start portions. Human intervention was required to clean the surfaces in these cases. In contrast, there were no non-welding moves in the Eulerian tool path, and the movement efficiency reached 100 %, requiring no human intervention.

Fig. 25 illustrates the metallic parts obtained using the standard and

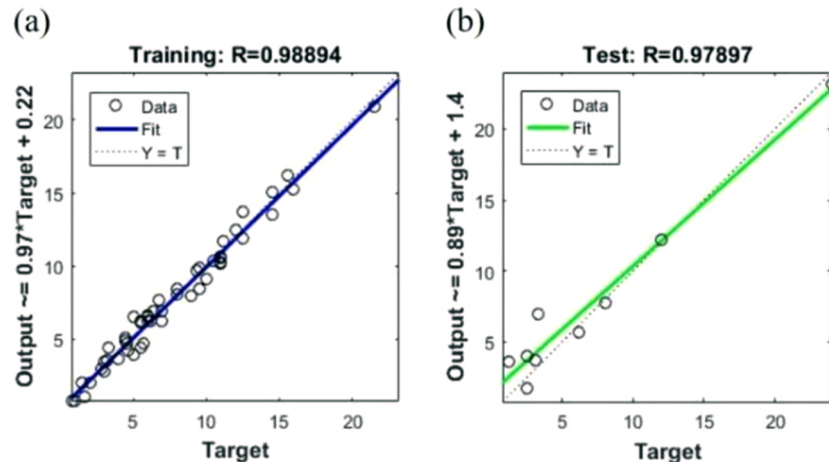


Fig. 22. Regression: (a) training; (b) test.

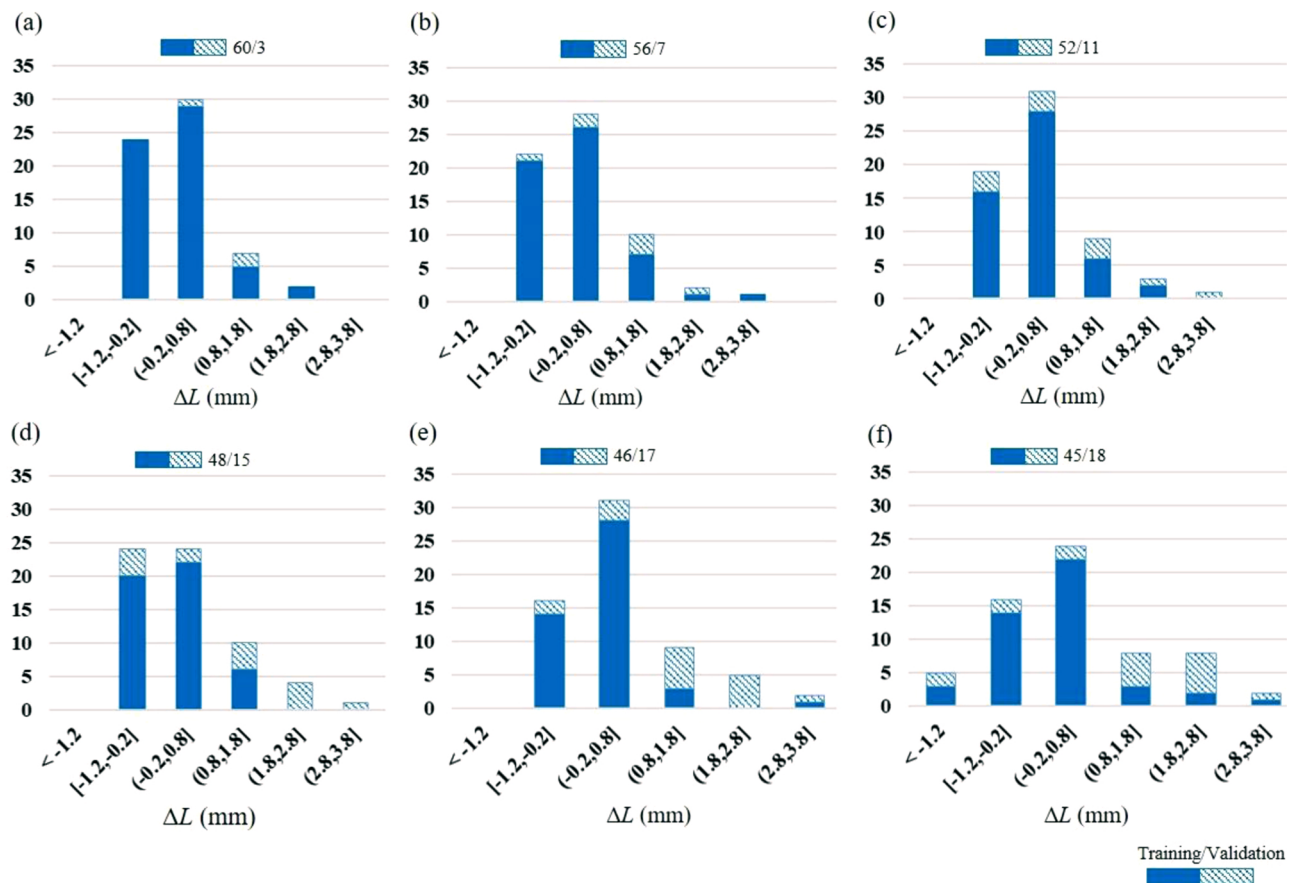


Fig. 23. Error histograms for various sets of training / validation data.

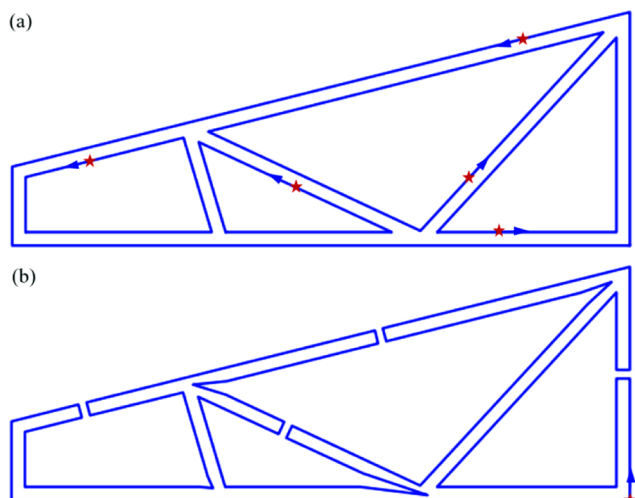


Fig. 24. Comparison of (a) the standard contour tool path and (b) the Eulerian tool path. The red stars show start/stop positions.

the Eulerian tool path. Tool paths and process parameters are reported in Fig. 24 and Table 3, respectively. A single weld bead geometry is 5.3 mm wide and 1.8 mm high. With two-overlapping weld beads, the wall thickness is about 9.0 mm. Both parts are about 45.0 mm high. The deposition rate is over 3.0 kg/h. The part welded with the standard tool path shows voids in every junction due to lack of material. The volumes needed to weld the junctions are greater than the volume deposited along the walls. Hence, the standard contour tool path is unable to fill up these areas. In addition, traces of the start and end positions (marked by red circles) can be found on the part because the end portion of weld

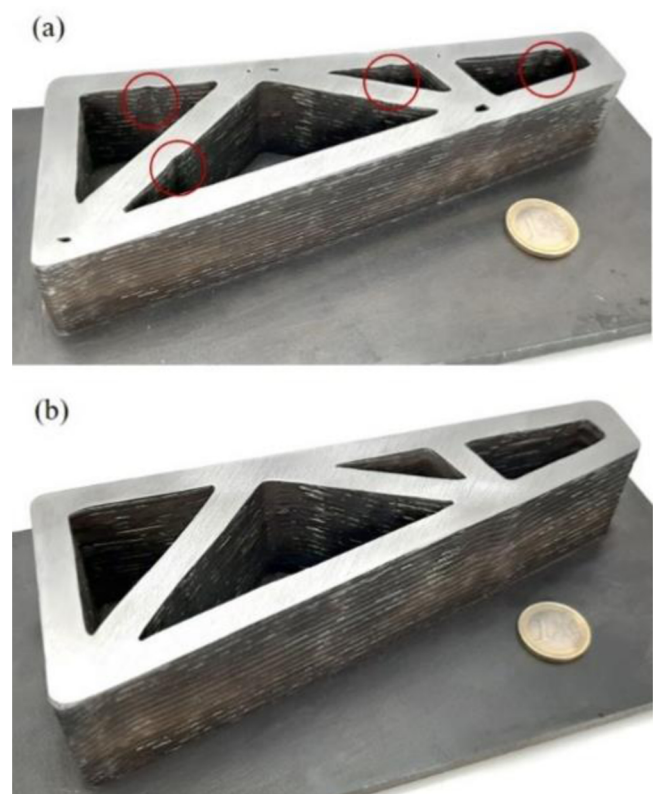


Fig. 25. Metallic parts after face milling: (a) standard tool path; (b) proposed tool path.

Table 5

The number of weld passes and processing time for one layer.

Tool path patterns	Weld passes	Processing time (second)
Traditional tool path	5	230
Proposed tool path	1	190

seams is usually smaller. With the developed strategy, the part shows no voids at the junctions.

Rib-web structures can be deposited with single weld beads. In general, however, this causes discontinuous weld paths with various non-welding motions. In this case, imperfections such as peak, voids or binding errors may appear at the junctions [38], and the rapid moves might reduce the movement efficiency. As mentioned above, the width of single weld beads limits the rib thickness to about 7.0 mm for the steel considered in this work. For thicker ribs, zigzag motion or multiple weld beads can be used. With zigzag welding motion, the surface roughness is worse than with contour paths [39], and a high possibility of warpage [12] occurs. The tool path strategy proposed in this work allows for continuous welding following Eulerian paths with multi-overlapping weld bead. In this case, defects may still occur in junctions and hence a correction of the tool path is necessary. The study explored a correction strategy that draws upon a step of the torch into the center of the junction, thus depositing material in the place, which may suffer from underfilling. It was shown that the correction step size, i.e. the length of the motion into the center of the junction, can be obtained by determining the underfilling that occurs when the part is welded without correction. It is a cumbersome process to determine the underfilling for each individual junction type.

The results presented above show that machine learning can be used to train a neural network that represents the correction as a function of the junction geometry. This network can be trained with 46 junction geometries of degree three and four. For higher connectivity of the junction, a larger number of experiments may be required. Nevertheless, it seems that for each material, a neural network can be trained that represents a suitable correction to avoid voids in junctions. In combination with the proposed strategy to derive Eulerian paths, a strategy for welding arbitrary rib-web geometries seems feasible. One limitation of the approach may arise from the fact that the network is trained to avoid voids in junctions but it allows peaks, i.e. excess material, to occur. This may limit the feasible build height. An improvement could be achieved by considering the peak height during training, i.e. by including additional information.

Moreover, it has to be noted that the method should be preferred when the desired wall thickness cannot be attained with a single bead, and may still be used otherwise if it yields a more stable process or improves the welding motion efficiency. Some parts may not be pure rib-web structures but combinations between rib-webs and bulky features. In this case, the method needs to be extended by accounting for transitions between the different part features. The method may also be applied to other direct energy deposition processes such as laser metal deposition or electron beam additive manufacturing. In this case, however, the deposition process is largely different from WAAM and other correction strategies such as re-melting of the junction seems feasible. As an alternative to experimental data, it seems at present infeasible to use simulated results. If particle methods are used, it may be possible to obtain accurate results for the form filling, but it will be much faster to conduct 46 experiments than the same number of simulations. Up to now, the goal of the continuous path is to avoid rapid moves and as well as multiple starts and stops on a layer. This method may, however, lead to unfavorable temperature gradients on a layer. Future work will thus analyze whether the random choice of locations for reversing the welding direction should be replaced by a method that takes, e.g., the temperature distribution into account.

4. Conclusions

This work presents an innovative tool path planning strategy for wire-arc additive manufacturing processes for rib-web lightweight structures. The main results can be summarized as follows:

- The algorithm proposed to perform the welding motion computes offset curves from the inner and outer part contours which serve as welding paths. Based on a strategy to connect these paths, the proposed algorithm is able to generate Eulerian paths from arbitrary connected rib-web geometries, which allows for continuous tool motion.
- The deposition process is continuous. The welding torch is turned on at the beginning of the process and remains switched on until the part is finished. Hence, uneven weld beads can be avoided.
- The movement efficiency reaches almost 100 % because it avoids non-welding moves entirely.
- To avoid defects in junctions, a geometrical correction strategy is proposed which aims at depositing precisely the amount of material required to generate the junction. It was found that due to the complex dependence of the deposition process in the junctions on junction geometry, material and process parameters, avoiding voids and peaks only based on a geometrical model is not feasible in general. Hence, a method was developed that allows for finding the optimal path correction for a given junction by welding this junction once with the geometrical correction, evaluating the void length, and updating the correction factor.
- If only a single geometry is produced in large quantities, optimization should draw upon this correction strategy. In variant-rich production, however, it may be tedious to optimize all junction types independently.
- To represent the knowledge for welding arbitrary junction types without defects, an adaptive void-filling strategy has been developed that draws upon an artificial neural network. Machine learning proved to provide an efficient means to capture the functional relations between the correction to be applied and the junction geometry.
- Categorization of the junctions and supervised learning were applied to identify an optimal training set of 46 junction geometries for junctions of degree of at most four. The 46 test geometries were used to train a neural network such that it made accurate predictions for 17 validation cases. With an effort of one day, sufficient information can be gathered that allows for welding other rib-web structures without defects.
- It has to be noted, however, that the methodology presented here may not be transferable directly to other materials and set-ups and that training with dedicated geometries welded with the given set-up may be necessary. Future work could include training sets in which also the welding parameters are varied.
- For the selected welding parameters, the proposed algorithm yields a deposition rate of over 3.0 kg/h.
- The proposed method can replace other tool path planning strategies for rib-web structures and may reduce the probability of welding defects and increase the welding movement efficiency.

There is a trade-off between the benefits of the adaptive-void filling tool path and the height of the junctions. The research has shown that it is not feasible to achieve void-free and absolutely flat surfaces in junctions. The higher the peak is, the smaller is the possibility of voids, and vice versa. The scope of this study was to minimize the voids. Future work could focus on strategies to avoid peaks emerging at junctions. To fully exploit the method, the mechanical properties and residual stresses have to be analyzed and taken into account in order to optimize the welding and tool path parameters.

Declaration of Competing Interest

The authors declare that there are no conflicts of interest.

Acknowledgements

This research did not receive any specific grant from funding agencies in the public, commercial, or not-for-profit sectors.

Appendix A. Full experimental data

No.	Group	Configuration					L_{Target} (mm)
		η	θ_1 (degree)	θ_2 (degree)	θ_3 (degree)	θ_4 (degree)	
1	A ₁	3	120	120	120	0	0.8
2	B ₁	2	180	90	90	0	1.0
3	B ₂	3	150	150	60	0	2.1
4	B ₃	3	160	160	40	0	2.5
5	B ₄	3	165	165	30	0	6.2
6	C ₁	3	150	120	90	0	1.2
7	C ₂	2	180	108	72	0	1.5
8	C ₃	2	180	120	60	0	1.6
9	C ₄	2	180	126	54	0	1.7
10	C ₅	2	180	144	36	0	2.5
11	C ₆	2	180	150	30	0	2.8
12	C ₇	2	180	162	18	0	6.8
13	C ₈	2	180	165	15	0	10.0
14	D ₁	4	90	90	90	90	3.0
15	E ₁	3	180	60	60	60	5.0
16	E ₂	4	135	75	75	75	4.0
17	E ₃	4	100	100	100	60	3.0
18	F ₁	4	108	72	108	72	4.6
19	F ₂	4	120	60	120	60	6.0
20	F ₃	4	126	54	126	54	3.3
21	F ₄	4	135	45	135	45	9.0
22	F ₅	4	144	36	144	36	9.5
23	F ₆	4	150	30	150	30	12.0
24	F ₇	4	162	18	162	18	24.5
25	F ₈	4	165	15	165	15	28.3
26	F ₉	4	108	72	72	108	3.1
27	F ₁₀	4	120	60	60	120	4.7
28	F ₁₁	4	126	54	54	126	3.3
29	F ₁₂	4	135	45	45	135	5.7
30	F ₁₃	4	144	36	36	144	4.8
31	F ₁₄	4	150	30	30	150	5.5
32	F ₁₅	4	162	18	18	162	10.5
33	F ₁₆	4	165	15	15	165	11.0
34	G ₁	3	180	52	76	52	6.0
35	G ₂	3	180	45	90	45	8.0
36	G ₃	3	180	37	106	37	11.0
37	G ₄	3	180	30	120	30	11.2
38	G ₅	3	180	90	45	45	4.5
39	G ₆	3	180	120	30	30	6.0
40	G ₇	4	108	90	90	72	3.2
41	G ₈	4	120	90	90	60	5.5
42	G ₉	4	126	90	90	54	4.5
43	G ₁₀	4	144	90	90	36	7.0
44	G ₁₁	4	150	90	90	30	9.5
45	G ₁₂	4	162	90	90	18	16.0
46	H ₁	3	180	90	60	30	8.0
47	H ₂	3	180	90	70	20	11.0
48	H ₃	3	180	90	30	60	5.5
49	H ₄	3	180	90	20	70	11.0
50	H ₅	3	180	15	30	135	11.0
51	H ₆	3	180	30	15	135	12.0
52	H ₇	4	126	72	108	54	6.2
53	H ₈	4	144	72	108	36	6.4
54	H ₉	4	144	54	126	36	8.0
55	H ₁₀	4	162	72	108	18	12.5
56	H ₁₁	4	162	54	126	18	14.5
57	H ₁₂	4	162	36	144	18	15.6
58	H ₁₃	4	126	108	72	54	4.6
59	H ₁₄	4	144	108	72	36	5.0
60	H ₁₅	4	144	126	54	36	7.0
61	H ₁₆	4	162	108	72	18	14.5
62	H ₁₇	4	162	126	54	18	12.5
63	H ₁₈	4	162	144	36	18	9.4

Appendix B. Training data

No.	Group	Input				L_{Target} (mm)	$L_{Predict}$ (mm)	$\Delta L = L_{Predict} - L_{Target}$ (mm)
		η	θ_1 (degree)	θ_2 (degree)	θ_3 (degree)	θ_4 (degree)		
1	A ₁	3	120	120	120	0	0.8	0.3
2	B ₁	2	180	90	90	0	1.0	0.1
3	B ₂	3	150	150	60	0	2.1	1.5
4	B ₃	3	160	160	40	0	2.5	3.6
5	B ₄	3	165	165	30	0	6.2	6.3
6	C ₁	3	150	120	90	0	1.2	1.8
7	C ₂	2	180	108	72	0	1.5	1.9
8	C ₃	2	180	120	60	0	1.6	2.0
9	C ₄	2	180	126	54	0	1.7	0.8
10	C ₅	2	180	144	36	0	2.5	1.5
11	C ₆	2	180	150	30	0	2.8	2.2
12	C ₇	2	180	162	18	0	6.8	6.0
13	C ₈	2	180	165	15	0	10.0	10.7
14	D ₁	4	90	90	90	90	3.0	3.5
15	E ₁	3	180	60	60	60	5.0	4.0
16	E ₂	4	135	75	75	75	4.0	3.0
17	E ₃	4	100	100	100	60	3.0	3.3
18	F ₁	4	108	72	108	72	4.6	5.2
19	F ₂	4	120	60	120	60	6.0	6.4
20	F ₃	4	126	54	126	54	3.3	3.5
21	F ₄	4	135	45	135	45	9.0	9.1
22	F ₅	4	144	36	144	36	9.5	8.4
23	F ₆	4	150	30	150	30	12.0	11.6
24	F ₈	4	165	15	165	15	28.3	27.5
25	F ₉	4	108	72	72	108	3.1	3.4
26	F ₁₀	4	120	60	60	120	4.7	4.6
27	F ₁₁	4	126	54	54	126	3.3	2.3
28	F ₁₂	4	135	45	45	135	5.7	8.1
29	F ₁₃	4	144	36	36	144	4.8	5.4
30	F ₁₄	4	150	30	30	150	5.5	5.0
31	F ₁₅	4	162	18	18	162	10.5	10.4
32	F ₁₆	4	165	15	15	165	11.0	11.5
33	G ₁	3	180	52	76	52	6.0	6.0
34	G ₂	3	180	45	90	45	8.0	9.5
35	G ₃	3	180	37	106	37	11.0	10.2
36	G ₄	3	180	30	120	30	11.2	10.6
37	G ₅	3	180	90	45	45	4.5	4.9
38	G ₆	3	180	120	30	30	6.0	5.6
39	G ₇	4	108	90	90	72	3.2	2.5
40	G ₈	4	120	90	90	60	5.5	6.7
41	G ₉	4	126	90	90	54	4.5	4.3
42	G ₁₀	4	144	90	90	36	7.0	6.2
43	G ₁₁	4	150	90	90	30	9.5	9.5
44	G ₁₂	4	162	90	90	18	16.0	16.2
45	H ₁	3	180	90	60	30	8.0	8.6
46	H ₂	3	180	90	70	20	11.0	11.1
47	H ₄	3	180	90	20	70	11.0	10.2
48	H ₅	3	180	15	30	135	11.0	11.7
49	H ₆	3	180	30	15	135	12.0	12.6
50	H ₇	4	126	72	108	54	6.2	7.0
51	H ₈	4	144	72	108	36	6.4	6.2
52	H ₉	4	144	54	126	36	8.0	9.5
53	H ₁₀	4	162	72	108	18	12.5	13.0
54	H ₁₁	4	162	54	126	18	14.5	14.2
55	H ₁₂	4	162	36	144	18	15.6	15.4
56	H ₁₃	4	126	108	72	54	4.6	7.1
57	H ₁₄	4	144	108	72	36	5.0	5.6
58	H ₁₆	4	162	108	72	18	14.5	15.1
59	H ₁₇	4	162	126	54	18	12.5	12.8
60	H ₁₈	4	162	144	36	18	9.4	9.1

Appendix C. Optimal training data

No.	Group	Input				Measureme- nt	$L_{Predict}$ (mm)	Prediction	Deviation
		η	θ_1 (degree)	θ_2 (degree)	θ_3 (degree)	θ_4 (degree)			
1	B ₁	2	180	90	90	0	1.0	1.51	0.5
2	B ₂	3	150	150	60	0	2.1	2.28	0.2
3	B ₃	3	160	160	40	0	2.5	2.56	0.1
4	B ₄	3	165	165	30	0	6.2	6.30	0.1
5	C ₁	3	150	120	90	0	1.2	1.58	0.4
6	C ₃	2	180	120	60	0	1.62	2.00	0.4
7	C ₄	2	180	126	54	0	1.7	1.37	-0.3
8	C ₅	2	180	144	36	0	2.5	3.01	0.5
9	C ₇	2	180	162	18	0	6.8	6.11	-0.7
10	C ₈	2	180	165	15	0	10.0	9.32	-0.7
11	D ₁	4	90	90	90	90	3.0	2.98	0.0
12	E ₁	3	180	60	60	60	5.0	6.49	1.5
13	E ₂	4	135	75	75	75	4.0	4.40	0.4
14	E ₃	4	100	100	100	60	3.0	3.38	0.4
15	F ₁	4	108	72	108	72	4.6	4.47	-0.1
16	F ₂	4	120	60	120	60	6.0	6.02	0.0
17	F ₄	4	135	45	135	45	9.0	8.17	-0.8
18	F ₇	4	162	18	162	18	24.5	24.60	0.1
19	F ₈	4	165	15	165	15	28.3	28.98	0.7
20	F ₉	4	108	72	72	108	3.1	3.60	0.5
21	F ₁₀	4	120	60	60	120	4.7	4.14	-0.6
22	F ₁₂	4	135	45	45	135	5.7	5.20	-0.5
23	F ₁₃	4	144	36	36	144	4.8	4.28	-0.5
24	F ₁₄	4	150	30	30	150	5.5	6.11	0.6
25	F ₁₆	4	165	15	15	165	11.0	11.31	0.3
26	G ₁	3	180	52	76	52	6.0	6.95	0.9
27	G ₂	3	180	45	90	45	8.0	8.23	0.2
28	G ₃	3	180	37	106	37	11.0	11.36	0.4
29	G ₇	4	108	90	90	72	3.2	3.41	0.2
30	G ₈	4	120	90	90	60	5.5	5.38	-0.1
31	G ₁₀	4	144	90	90	36	7.0	6.57	-0.4
32	G ₁₁	4	150	90	90	30	9.5	9.80	0.3
33	G ₁₂	4	162	90	90	18	16.0	17.06	1.1
34	H ₁	3	180	90	60	30	8.0	7.93	-0.1
35	H ₂	3	180	90	70	20	11.0	11.09	0.1
36	H ₃	3	180	90	30	60	5.5	5.24	-0.3
37	H ₄	3	180	90	20	70	11.0	10.93	-0.1
38	H ₅	3	180	15	30	135	11.0	10.37	-0.6
39	H ₆	3	180	30	15	135	12.0	11.80	-0.2
40	H ₇	4	126	72	108	54	6.2	6.21	0.0
41	H ₉	4	144	54	126	36	8.0	8.45	0.4
42	H ₁₂	4	162	36	144	18	15.6	14.36	-1.2
43	H ₁₄	4	144	108	72	36	5.0	4.95	-0.1
44	H ₁₅	4	144	126	54	36	7.0	6.48	-0.5
45	H ₁₆	4	162	108	72	18	14.5	17.92	3.4
46	H ₁₇	4	162	126	54	18	12.5	12.14	-0.4
47	A ₁	3	120	120	120	0	0.8	1.91	1.1
47	C ₂	2	180	108	72	0	1.5	1.53	0.0
49	C ₆	2	180	150	30	0	2.8	4.34	1.5
50	F ₃	4	126	54	126	54	3.3	7.17	3.9
51	F ₅	4	144	36	144	36	9.5	11.29	1.8
52	F ₆	4	150	30	150	30	12	14.12	2.1
53	F ₁₁	4	126	54	54	126	3.3	5.01	1.7
54	F ₁₅	4	162	18	18	162	10.5	9.59	-0.9
55	G ₄	3	180	30	120	30	11.2	12.11	0.9
56	G ₅	3	180	90	45	45	4.5	7.25	2.7
57	G ₆	3	180	120	30	30	6.0	8.30	2.3
58	G ₉	4	126	90	90	54	4.5	5.13	0.6
59	H ₈	4	144	72	108	36	6.4	7.44	1.0
60	H ₁₀	4	162	72	108	18	12.5	14.99	2.5
61	H ₁₁	4	162	54	126	18	14.5	14.00	-0.5
62	H ₁₃	4	126	108	72	54	4.6	4.85	0.2
63	H ₁₈	4	162	144	36	18	9.4	11.80	2.4

References

- [1] P.S. Almeida, S. Williams, Innovative process model of Ti-6Al-4V additive layer manufacturing using cold metal transfer (CMT), Proceedings of the Twenty-First Annual International Solid Freeform Fabrication Symposium, University of Texas at Austin, Austin, TX, USA, 2010.
- [2] L. Nguyen, J. Buhl, M. BAMBACH, Decomposition algorithm for tool path planning for wire-arc additive manufacturing, *J. Mach. Eng.* 18 (2018).
- [3] Y. Javadi, C.N. MacLeod, S.G. Pierce, A. Gachagan, D. Lines, C. Mineo, J. Ding, S. Williams, M. Vasilev, E. Mohseni, R. Su, Ultrasonic phased array inspection of a Wire + Arc Additive Manufactured (WAAM) sample with intentionally embedded

- defects, *Addit. Manuf.* 29 (2019) 100806, , <https://doi.org/10.1016/j.addma.2019.100806>.
- [4] P.F. Bariami, G. Berti, L. D'Angelo, Tool cost estimating at the early stages of cold forging process design, *CIRP Ann. Manuf. Technol.* 42 (1993) 279–282, [https://doi.org/10.1016/S0007-8506\(07\)62443-3](https://doi.org/10.1016/S0007-8506(07)62443-3).
- [5] J. Allen, *An Investigation Into the Comparative Costs of Additive Manufacture vs. Machine From Solid for Aero Engine Parts*, (2006).
- [6] P. Colegrave, C. Ikeagu, A. Thistlethwaite, S. Williams, T. Nagy, W. Suder, A. Steuwer, T. Pirling, Welding process impact on residual stress and distortion, *Sci. Technol. Weld. Join.* 14 (2013) 717–725, <https://doi.org/10.1179/136217109X406938>.
- [7] M.S. Anwar, S.P. Untawale, Measuring the process efficiency of controlled welding processes, *Int. J. Instrum. Control Autom.* 1 (2012) 33–39.
- [8] S. Katayama, Defect formation mechanisms and preventive procedures in laser welding, *Handbook of Laser Welding Technologies*, Elsevier, 2013, pp. 332–373.
- [9] Y. Zhang, Y. Chen, P. Li, A.T. Male, Weld deposition-based rapid prototyping: a preliminary study, *J. Mater. Process. Technol.* 135 (2003) 347–357, [https://doi.org/10.1016/S0924-0136\(02\)00867-1](https://doi.org/10.1016/S0924-0136(02)00867-1).
- [10] K.P. Karunakaran, S. Suryakumar, U. Chandrasekhar, A. Bernard, Hybrid rapid manufacturing of metallic objects, *IJRapidM* 1 (2010) 433, <https://doi.org/10.1504/IJRapidM.2010.036116>.
- [11] G. Ma, G. Zhao, Z. Li, M. Yang, W. Xiao, Optimization strategies for robotic additive and subtractive manufacturing of large and high thin-walled aluminum structures, *Int. J. Adv. Manuf. Technol.* 52 (2018) 589, <https://doi.org/10.1007/s00170-018-3009-3>.
- [12] D. Eisenbarth, F. Wirth, K. Spieldiener, K. Wegener, Enhanced toolpath generation for direct metal deposition by using distinctive CAD data, *International Conference on Additive Manufacturing in Products and Applications* (2017) 152–161.
- [13] G.Q. Jin, W.D. Li, L. Gao, An adaptive process planning approach of rapid prototyping and manufacturing, *Robot. Comput. Manuf.* 29 (2013) 23–38, <https://doi.org/10.1016/j.rcim.2012.07.001>.
- [14] D. Ding, Z. Pan, D. Cuiuri, H. Li, S. van Duin, N. Larkin, Bead modelling and implementation of adaptive MAT path in wire and arc additive manufacturing, *Robot. Comput. Manuf.* 39 (2016) 32–42, <https://doi.org/10.1016/j.rcim.2015.12.004>.
- [15] J. Mehnen, J. Ding, H. Lockett, P. Kazanas, Design for wire and arc additive layer manufacture, *Global Product Development*, Springer, 2011, pp. 721–727.
- [16] G. Venturini, F. Montevercchi, A. Scippa, G. Campatelli, Optimization of WAAM deposition patterns for T-crossing features, *Procedia CIRP* 55 (2016) 95–100, <https://doi.org/10.1016/j.procir.2016.08.043>.
- [17] G. Venturini, F. Montevercchi, F. Bandini, A. Scippa, G. Campatelli, Feature based three axes computer aided manufacturing software for wire arc additive manufacturing dedicated to thin walled components, *Addit. Manuf.* 22 (2018) 643–657, <https://doi.org/10.1016/j.addma.2018.06.013>.
- [18] P. Chebolu, M. Cryan, R. Martin, Exact counting of Euler tours for generalized series-parallel graphs, *J. Discret. Algorithms* 10 (2012) 110–122, <https://doi.org/10.1016/j.jda.2011.03.011>.
- [19] Neto, Leonor Machado Santos Carvalho, *Studying the Application of Additive Manufacturing to Large Parts*, Universidade de Lisboa, 2017.
- [20] S. Suryakumar, K.P. Karunakaran, A. Bernard, U. Chandrasekhar, N. Raghavender, D. Sharma, Weld bead modeling and process optimization in hybrid layered manufacturing, *Comput. Des.* 43 (2011) 331–344.
- [21] B. Chan, J. Pacey, M. Bibby, Modelling gas metal arc weld geometry using artificial neural network technology, *Can. Metall. Q.* 38 (1999) 43–51, <https://doi.org/10.1179/cmq.1999.38.1.43>.
- [22] J.E. Pinto-Lopera, J.M. ST Motta, S.C. Absi Alfaro, Real-time measurement of width and height of weld beads in GMAW processes, *Sensors* 16 (2016) 1500.
- [23] J. Xiong, G. Zhang, J. Hu, L. Wu, Bead geometry prediction for robotic GMAW-based rapid manufacturing through a neural network and a second-order regression analysis, *J. Intell. Manuf.* 25 (2012) 157–163.
- [24] F. Martina, J. Mehnen, S.W. Williams, P. Colegrave, F. Wang, Investigation of the benefits of plasma deposition for the additive layer manufacture of Ti-6Al-4V, *J. Mater. Process. Technol.* 212 (2012) 1377–1386, <https://doi.org/10.1016/j.jmatprote.2012.02.002>.
- [25] D. Ding, Z. Pan, D. Cuiuri, H. Li, Process planning for robotic wire and arc additive manufacturing, *Industrial Electronics and Applications (ICIEA)*, 2015 IEEE 10th Conference on, 2015, pp. 2000–2003.
- [26] A.W. Society, AWS A 5.18: specification for carbon steel electrodes and rods for gas shielded arc welding, AWS Miami (2005).
- [27] DIN EN 10083-1, 2006th ed., Deutsches Institut fur Normung E.V. (DIN).
- [28] H. Nagamatsu, H. Sasahara, Y. Mitsutake, T. Hamamoto, Development of a co-operative system for wire and arc additive manufacturing and machining, *Addit. Manuf.* 31 (2020) 100896, , <https://doi.org/10.1016/j.addma.2019.100896>.
- [29] A. Adebayo, *Characterisation of Integrated WAAM and Machining Processes*, (2013).
- [30] D. Weisz-Patrault, Fast simulation of temperature and phase transitions in directed energy deposition additive manufacturing, *Addit. Manuf.* 31 (2020) 100990, , <https://doi.org/10.1016/j.addma.2019.100990>.
- [31] FANUC Robot series, R-30iB Mate CONTROLLER, (2020).
- [32] A. Thompson, I. Maskery, R.K. Leach, X-ray computed tomography for additive manufacturing: a review, *Meas. Sci. Technol.* 27 (2016) 72001.
- [33] J.A. Slotwinski, E.J. Garboczi, K.M. Hebenstreit, Porosity measurements and analysis for metal additive manufacturing process control, *J. Res. Inst. Stand. Technol.* 119 (2014) 494–528, <https://doi.org/10.6028/jres.119.019>.
- [34] F. Burden, D. Winkler, Bayesian regularization of neural networks, *Artificial Neural Networks*, Springer, 2008, pp. 23–42.
- [35] S. Jhavar, N.K. Jain, C.P. Paul, Development of micro-plasma transferred arc (μ -PTA) wire deposition process for additive layer manufacturing applications, *J. Mater. Process. Technol.* 214 (2014) 1102–1110, <https://doi.org/10.1016/j.jmatprote.2013.12.016>.
- [36] A. Krizhevsky, I. Sutskever, G.E. Hinton, Imagenet classification with deep convolutional neural networks, *Adv. Neural Inf. Process. Syst.* (2012) 1097–1105.
- [37] O. Maimon, L. Rokach, *Soft Computing for Knowledge Discovery and Data Mining*, Springer, US, Boston, MA, 2008.
- [38] J. Mehnen, J. Ding, H. Lockett, P. Kazanas, Design study for wire and arc additive manufacture, *IJPD* 19 (2014) 2, <https://doi.org/10.1504/IJPD.2014.060028>.
- [39] D. Ding, Z.S. Pan, D. Cuiuri, H. Li, A tool-path generation strategy for wire and arc additive manufacturing, *Int. J. Adv. Manuf. Technol.* 73 (2014) 173–183.